A Facile Low-Temperature Approach to Designing Controlled Amorphous-Based Titania Composite Photocatalysts with Excellent Noble-Metal-Free Photocatalytic Hydrogen Production

Si-yao Guo,[†,‡] Song Han,*[,‡] Bo Chi,[†] Jian Pu,[†] and Jian Li[†]

[†]School of Materials Science and Engineering, State Key Lab of Material Processing and Die & Mould Technology, Huazhong University of Science and Technology, Wuhan 430074, China

[‡]College of Forestry, Northeast Forestry University, Harbin 150040, China

Ⓢ Supporting Information

ABSTRACT: A microporous amorphous-based titania composite photocatalysts has been fabricated using a facile low-temperature (120 °C) synthetic method. Notably, we have successfully prepared the various stages of the amorphous/crystalline heterostructure by simply adjusting the pH value. The high-pH sample favors the formation of amorphous based titania composite structure. Additionally, the BET surface area of the sample increases with the increasing of the pH value, reaching a maximum of 358 m^2 g^{-1} when the pH value is 12. Unexpectedly, the H_2 productivity of amorphous-based composite photocatalyst without noble metal co-catalyst increases significantly with the increasing pH value, which is attributed to the quickly increasing amorphous, and the highly active catalytic centers created by the synergistic effect between crystalline TiO_2 and amorphous ZnO. This study demonstrates that it is possible to improve the properties of the amorphous-based composite photocatalyst by properly modifying the synthesis conditions. The approach presented herein can be applied to the research of controlled amorphous-based composite photocatalytic systems.

KEYWORDS: noble-metal-free, amorphous-based, water-splitting, pH value
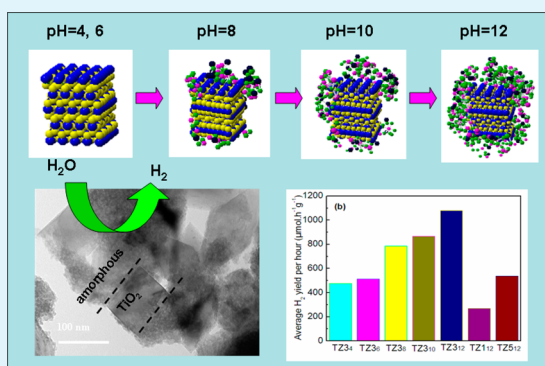
1. INTRODUCTION

Photocatalytic water-splitting has attracted great interest because the efficient generation of hydrogen using solar light can serve as a renewable energy resource.[1−4] Titania has been widely used in photocatalystic water splitting because of its low price, facile synthesis, and high chemical stability.[5−11] However, because of the low separation efficiency of the photoexcited charge carriers, most titania photocatalysts exhibits low efficiency or instability for photocatalystic water splitting. Ion doping, surface modification, and the use of different hybrid heterostructures have been used to improve the performance of photocatalysts.[12−20] Among these approaches, hybrid semiconductor heterostructures have been recognized as an effective route for improving the photocatalytic activity of TiO_2 because of their excellent performance in extending the light response and improving the separation of photogenerated electrons and holes in comparison with single-phase photocatalysts.[21−23] Heterostructures composed of coupled titania and zinc oxide have attracted great interest in recent years due to their similar structures and effective photocatalystic activity.[24,25] Because of the potential applications in advanced devices and systems, titania and zinc oxide are considered as two kinds of important semiconductors, and zinc oxide is also an appropriate alternative to titania due to its photodegradation mechanism

is similar to that of TiO_2. Therefore, nanocomposites of ZnO/TiO_2 can be a more powerful photocatalysts under solar irradiation in aqueous system.[26,27] The previously reported ZnO/TiO_2 composite photocatalysts usually combine crystalline ZnO with crystalline TiO_2 to form core−shell structures or other heterostructures.[28−30] Moreover, amorphous have been applied in many fields because it owns unique electronic structures,[31,32] and it has been reported that different crystal structures of ZnO/TiO_2 composite photocatalyst can be obtained by modified the Ti/Zn ratio, it is found that it will create a effective catalytic center for ZnO/TiO_2 heterostructure when ZnO is amorhous state.[11] And some researchers also reported that combining crystals with amorphous materials will improve the catalytic performance in many fields because of a synergistic action between them.[33−35] Therefore, further study of the ZnO/TiO_2 composite is of great interest, especially using ZnO in amorphous state.

Furthermore, because of porosity and BET surface area facilitates electron transfer and provides a plenty interface for reactions, thus it also play an important role in improving the

photocatalyst activity.[36] For water-splitting, using two different semiconductor photocatalysts, the increased lifetime of the photoproduced pairs due to the photogenerated hole and electron transfer between the two coupled semiconductors is invoked in many cases as the key factor for the photoactivity improvement. Thus, the photocatalytic activities strongly rely on the surface physicochemical properties, such as the type of phases, the porosity, and the surface area.

Generally, most photocatalytic water-splitting requires noble metal co-catalysts for photocatalytic hydrogen generation because noble metals can promote effective charge separation. However, using noble metals increases the cost of the catalyst, thus it is unsuitable for large-scale production and application. Unexpectedly, we found a facile low-temperature method for the in situ synthesis of microporous amorphous ZnO based titania composite catalysts with amorphous/crystalline structure. This novel photocatalyst configuration exhibits excellent photocatalytic activity for hydrogen evolution from photocatalystic water splitting without noble metal co-catalyst. Moreover, we also identified the transformation of the amorphous/crystalline heterostructure by adjusting the pH value.

2. EXPERIMENTAL SECTION

2.1. Catalyst Preparation. The detailed experimental description can refer to the previous paper.[11] Here, we fixed the pH value of 12 using a sodium hydroxide solution, and adjusted the TiO_2/ZnO molar ratios to 1/1, 3/1, and 5/1. These samples were marked as $TZ1_{12}$, $TZ3_{12}$ and $TZ5_{12}$ according to the Ti/Zn molar ratio and pH value (Ti/Zn = 1, 3, 5; pH 12). Moreover, we also fixed the Ti/Zn ratio of 3/1, and adjusted the pH value from 4, 6, 8, 10, and 12 using hydrochloric acid and sodium hydroxide solutions. These samples were marked as $TZ3_4$, $TZ3_6$, $TZ3_8$, $TZ3_{10}$, and $TZ3_{12}$ according to their Ti/Zn molar ratio and pH value (Ti/Zn = 3; pH 4, 6, 8, 10, and 12). Pure TiO_2 and ZnO were prepared by the same procedure without the addition of Zn and Ti source.

2.2. Characterization Techniques. X-ray diffraction patterns were performed on a Rigaku D/max-2200VPC diffractometer, and N_2 adsorption/desorption isotherms were tested by a Micromeritics ASAP 2020 surface area. The BET surface area was recorded using the Brunauer-Emmett-Teller (BET) method. Transmission electron microscopy (TEM) images were tested by a JEOL-JEM 2010 field emission transmission electron microscope. X-ray photoelectron spectroscopy (XPS) was recorded by a Shimadzu ESCA 750 instrument. The UV−vis spectra were obtained by a Perkin-Elmer Lambda. The FT-IR spectra were recorded on a Bruker Vertex 70 FT-IR spectrometer. Mass spectrometry was applied to measure hydrogen using a Pfeiffer OmniStar/ThermoStar GSD 320 instrument. The photocatalytic H_2 evolution experiments were tested on a LABSOLAR II apparatus (Beijing Perfectlight Technology Co. Lte). The light source is a 300 W xenon lamp (PLS-SEX-300C), which can simulate solar light irradiation.

2.3. H_2 Evolution Test. The photocatalytic H_2 evolution experiments were carried out on a LABSOLAR II photocatalytic water-splitting testing system. When it connected with the mass spectrometer, the mass spectrometer can realize the evolution of H_2 and analysis online, as shown in Figure 1. Typically, 10 mg of samples and 10 mL of methanol were mixed in 90 mL of aqueous solution. Before the start of the reaction, the air in the system was removed by a pump, and the H_2 evolved was periodically analyzed by a mass spectrometer.

3. RESULTS AND DISCUSSION

3.1. Crystal Structure, Morphology, and Porosity. Figure 2a shows the XRD spectra of $TZ1_{12}$, $TZ3_{12}$, and $TZ5_{12}$. The XRD pattern of $TZ1_{12}$ is showed pure amorphous

Figure 1. Photocatalytic water-splitting testing system.

state. Interestingly, for $TZ3_{12}$, an obviously amorphous peak can be observed besides the characteristic peaks of anatase, implying the existence of an amorphous/crystalline composite structure of the samples. In contrast, for $TZ5_{12}$, there exists only crystalline anatase phase, and the (101) diffraction peak is shifted to slightly lower angles compared to that of $TZ3_{12}$ (inset of Figure 2a), suggesting the expansion of the TiO_2 lattice. This expansion could result from the partial doping of Zn cations into the TiO_2 lattice by replacing the Ti sites in the lattice when the Ti/Zn ratio was 5/1. Because the cationic radius of Zn^{2+} (0.74 Å) is slightly larger than that of Ti^{4+} (0.61 Å), the partial replacement of Ti^{4+} with Zn^{2+} will result in lattice expansion and increase the lattice spacing. Fig. 2b shows the XRD patterns of $TZ3_4$, $TZ3_6$, $TZ3_8$, $TZ3_{10}$, and $TZ3_{12}$. It can be found that all the samples exhibit a completely anatase phase, without any ZnO or other impurities. However, for $TZ3_8$, $TZ3_{10}$, and $TZ3_{12}$, the XRD patterns show the mixed diffraction peaks of the amorphous/crystalline composite structure. The broadened amorphous peaks are increasingly evident with increasing pH. However, there is no visible amorphous peak in the XRD pattern when the pH value is 4 and 6. Therefore, the phase composition of the intrinsic crystal structure is strongly dependent on the pH value. At higher pH values, the formation of amorphous/crystalline composite structures is favored; conversely, under weakly acidic conditions, the formation of pure anatase is favored, which is consistent with the TEM analysis.

As shown in Figure 3, there are two binding energies (BEs) on the Zn 2p3/2 of $TZ1_{12}$ and $TZ3_{12}$, that is 1021.8 and 1021.7 eV, which belong to the characteristic peak of ZnO.[37] However, the XRD patterns only feature an amorphous peak for the anatase phase, with no characteristic peaks of crystalline ZnO; therefore, we deduce that the amorphous parts of the heterostructure are mainly composed of ZnO. The binding energy of $TZ5_{12}$ can be marked 1021.3 eV, which is caused by the doping of Zn^{2+} into the TiO_2 lattice with the formation of Zn−O−Ti bonds.[38] Because the electronegativity is different between Zn and Ti (Zn>Ti), the Zn 2p3/2 of $TZ5_{12}$ showed a negative shift. The O 1s of $TZ1_{12}$, $TZ3_{12}$, and $TZ3_{12}$ can be fitted by three peaks. The peaks at 529.5, 529.6, and 529.9 eV correspond to the Ti−O bonds, and the peaks at 531.6, 531.5, and 531.1 eV correspond to the Zn−O bonds.[39] The Ti 2p XPS spectrum is showm in Figure S1 in the Supporting Information. Compared to the Zn 2p XPS spectrum, the BE of $TZ5_{12}$ shows
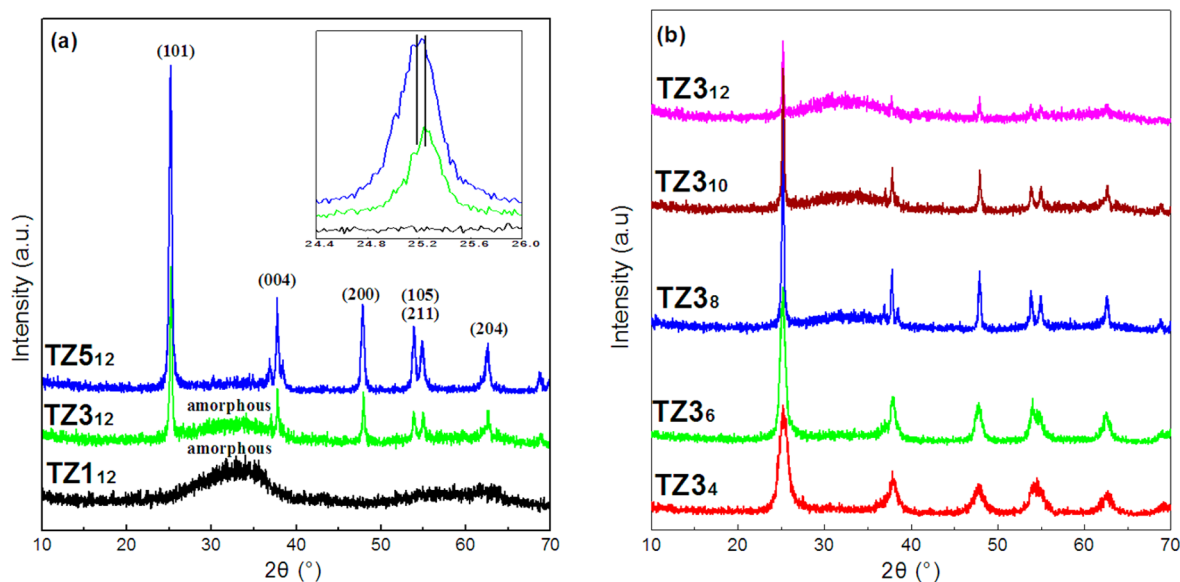
Figure 2. XRD patterns of the prepared samples: (a) $TZ1_{12}$, $TZ3_{12}$, and $TZ5_{12}$; (b) $TZ3_4$, $TZ3_6$, $TZ3_8$, $TZ3_{10}$, and $TZ3_{12}$.
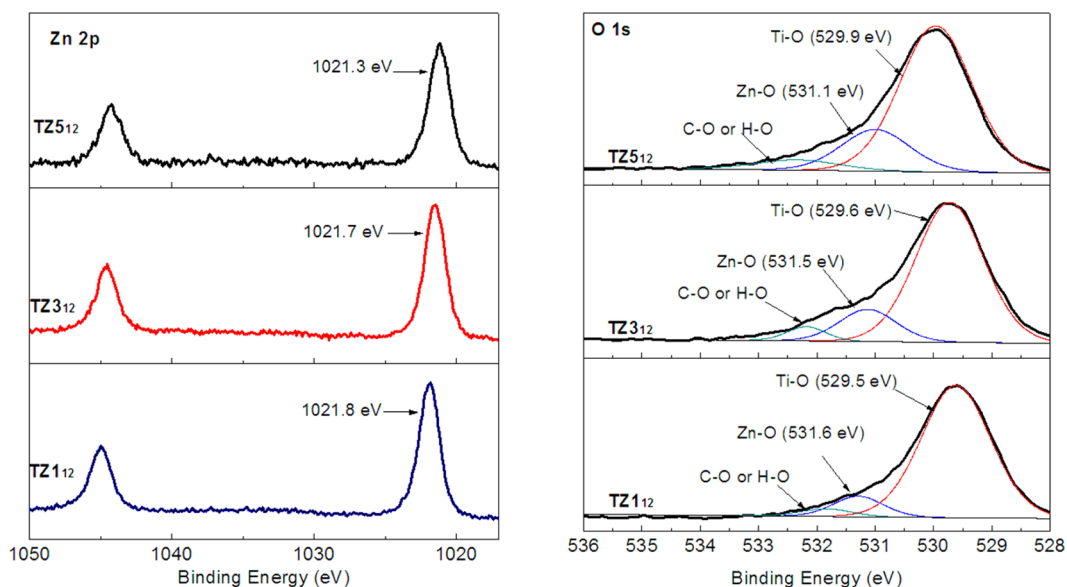

Figure 3. Zn 2p and O 1s XPS spectra of the $TZ1_{12}$, $TZ3_{12}$, and $TZ5_{12}$ samples.

a positive shift, which further confirmed the formation of Ti–O–Zn bonds.

TEM images of $TZ1_{12}$, $TZ3_{12}$, and $TZ5_{12}$ are shown in Figure 4. As shown in Figure 4a, $TZ1_{12}$ contains irregular particles approximately 50 nm in size, which is composed of amorphous based on corresponding SAED result. In Figure 4b, it is interesting to note that crystalline TiO_2 is clearly visible and surrounded by copious amounts of amorphous ZnO. The TEM image of $TZ5_{12}$ is shown in Figure 4c. The sample has a well-crystallized tetragonal shape, and no amorphous phase can be observed in the TEM or SAED patterns. Figure 4d shows the evolution of the crystal structure of the ZnO/TiO_2 composites, indicating that the crystalline structures of the sample with different Ti/Zn ratios undergo an amorphous, amorphous/crystalline and crystalline transition. The description of the crystal structure is shown in Figure S2 in the Supporting Information.

Figure 5 shows the TEM images of the ZnO/TiO_2 composites for various pH values. When the pH value is 4 or 6, crystalline TiO_2 can be obtained, and no amorphous phase can be found. When the pH value is 8, a small quantity of amorphous ZnO appears around the TiO_2. When the pH value is 10 or 12, the amorphous ZnO surrounding the TiO_2 becomes thicker and more compact. Figure 5f shows the HRTEM image of the black circle in the $TZ3_{12}$ image. The HRTEM reveals clear lattice fringes and a lattice spacing of approximately 0.351 nm, corresponding to the (101) plane of anatase. In addition, there are some low-intensity points in the image, indicating that there exist a lot of defects in the heterostructure. This can be further confirmed by the corresponding filtered image (the left image in Figure 5f), there are extensive defects on the filtered image, which could help to improve the photocatalytic activity. Figure 5g shows the evolution of the crystal structure of the ZnO/TiO_2 composites with different pH values, indicating that the crystal structure of
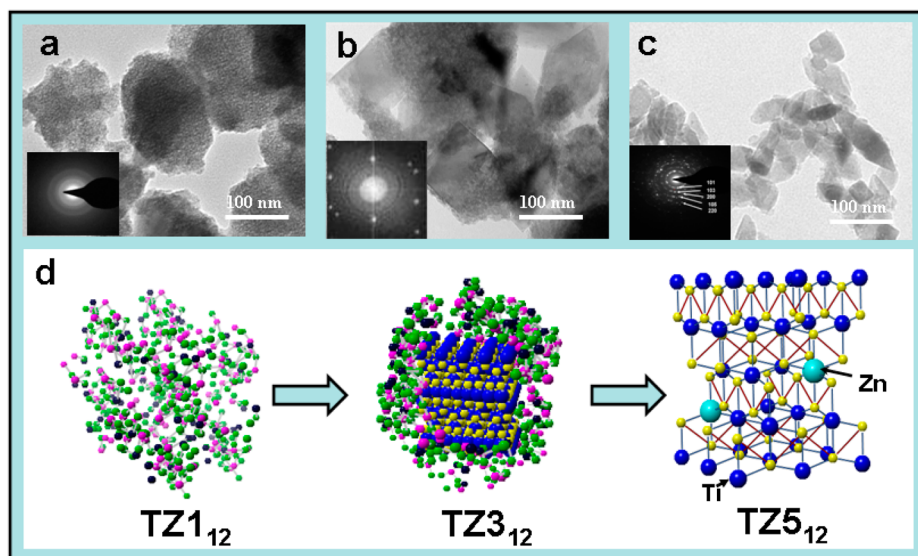
Figure 4. TEM images of (a) TZ1$_{12}$, (b) TZ3$_{12}$, and (c) TZ5$_{12}$. (d) Crystal structure of the ZnO/TiO$_2$ composites with various Ti/Zn ratios.
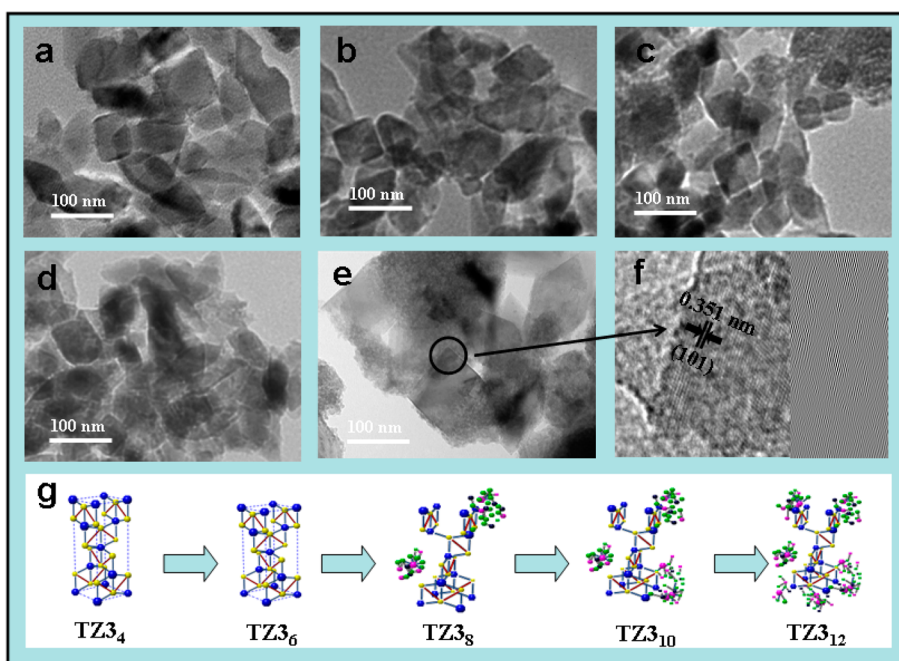
Figure 5. TEM images of ZnO/TiO$_2$ composites with various pH values: (a) TZ3$_4$, (b) TZ3$_6$, (c) TZ3$_8$, (d) TZ3$_{10}$, and (e) TZ3$_{12}$. (f) HRTEM image of the black circle in e, where the left image is the filtered image. (g) Crystal structure of the ZnO/TiO$_2$ composites at various pH values.
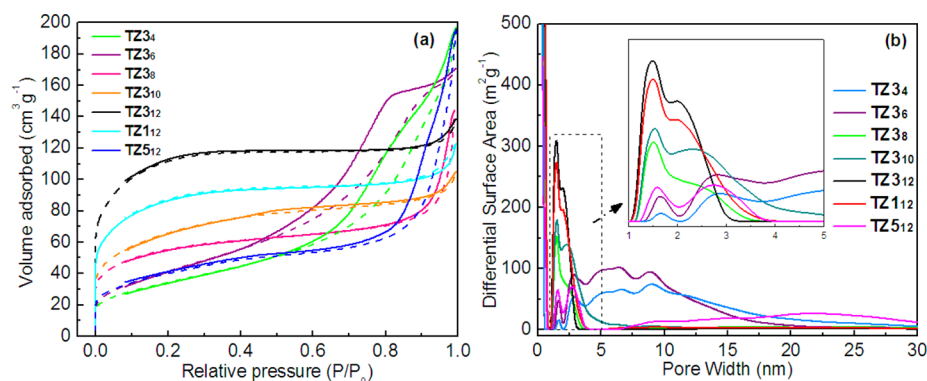

Figure 6. (a) N$_2$ adsorption−desorption isotherms and (b) pore size distribution of the prepared samples.

4746

dx.doi.org/10.1021/am4054095 | ACS Appl. Mater. Interfaces 2014, 6, 4743−4751

Table 1. Summary of the Properties of the Samples

sample	BET[a] ($m^2 g^{-1}$)	micropore area[b] ($m^2 g^{-1}$)	pore size[c] (nm)	pore volume[d] ($cm^3 g^{-1}$)	crystalline structure	H_2 evolution ($\mu mol\ h^{-1}\ g^{-1}$)
$TZ3_4$	124		9.8	0.31	anatase	475
$TZ3_6$	153		6.8	0.26	anatase	514
$TZ3_8$	181	13.6	4.9	0.22	amorphous/anatase	786
$TZ3_{10}$	222	48.8	2.9	0.14	amorphous/anatase	868
$TZ3_{12}$	358	143.3	2.3	0.19	amorphous/anatase	1081
$TZ1_{12}$	280	105.9	2.7	0.18	amorphous	270
$TZ5_{12}$	136	13.6	8.7	0.29	anatase	536

[a]Determined using the Brunauer−Emmett−Teller (BET) equation. [b]T-plot micropore area. [c]Adsorption average pore width (4 V/A by BET). [d]Single-point adsorption total pore volume of pores at $P/P_0 = 0.99$ rates (b).

the ZnO/TiO$_2$ composites tends to form a crystalline structure (anatase) for low pH values, and the characteristics of the amorphous/crystalline composite becomes more evident at higher pH values, which is consist with the XRD results.

To yield further insights into the specific surface area and porosity of the as-prepared TiO$_2$/ZnO heterostructure photocatalyst, N$_2$ adsorption−desorption measurements were tested. Figure 6a displays the N$_2$ adsorption−desorption isotherms of the samples. It is shown that TZ3$_4$ and TZ3$_6$ samples exhibit Type IV isotherms, and their BET specific surface areas are 124 and 153 m^2 g^{-1}, respectively. In contrast, the isotherms of TZ3$_8$, TZ3$_{10}$, TZ3$_{12}$, and TZ1$_{12}$ belong to the typical Type I isotherms, implying that the sample is a kind of microporous material. The micropore areas increase with the increase of the pH value. The pore size distributions are shown in Figure 6b. The high-pH sample has a main pore size distribution of ∼1.6 nm, whereas the maximum pore sizes of the samples shifted into larger mesoporous regions when the pH value is 4 or 6. The pore size distributions are obtained by density functional theory (DFT).[40] The BET surface area, micropore area, pore size and pore volume are summarized in Table 1, which indicates that the BET surface area of the sample increases significantly with the increasing of the pH value. Moreover, the sample with an amorphous structure (TZ1$_{12}$) is microporous, while the sample with a crystalline anatase structure (TZ5$_{12}$) is mesoporous. It is interesting to note that the samples with an amorphous/crystalline heterostructure (TZ3$_8$, TZ3$_{10}$, TZ3$_{12}$) also form microporous structures. On the basis of the above analysis, the large amounts of the amorphousness is likely responsible for the large BET surface area of the sample with an amorphous/crystalline composite structure.

3.2. FTIR Analysis. FTIR analysis was used to reveal the differences in the vibrational properties for different proportions of the ZnO/TiO$_2$ composite nanoparticles. Figure 7
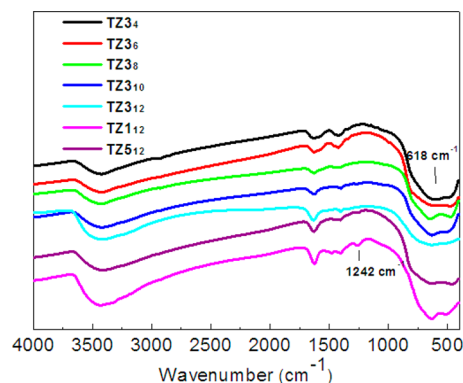
shows the FTIR spectra of the prepared samples. The broad bands at 3400 and 1630 cm^{-1} are related to surface-adsorbed water and hydroxyl groups, respectively.[41] These bands become slightly stronger as the Ti ratio increases, indicating that a higher Ti ratio could contribute to increasing the hydroxyl groups and surface-adsorbed water of titania. The bands at 1404 and 1242 cm^{-1} can be assigned to the symmetric stretches of the Ti−O bond and Ti−OH bond, respectively.[42−44] The bands at approximately 618 and 456 cm^{-1} are attributed to the vibration mode of the O−Ti−O band corresponding to the anatase crystalline titania.[45−48]

3.3. UV−Vis Analysis. Figure 8a shows the UV−vis absorption bands for the samples prepared with various Ti/Zn ratios. The absorption bands of the control samples (pure TiO$_2$ and ZnO) are located at 380.1 and 377.8 nm. The TZ1$_{12}$ sample, which has a pure amorphous structure, shows one sharp edges at 337.4 nm. However, for the TZ3$_{12}$ sample, which has an amorphous/crystalline composite structure, it is interesting to note that two absorption edges are located at 345.6 and 376.3 nm. In contrast with the TZ1$_{12}$ sample, we deduce that the absorption edges at 345.6 and 376.3 nm result from the amorphous and amorphous/crystalline composite structure, respectively. In contrast, for the TZ5$_{12}$ sample, which has a crystalline structure, the only absorption peak present is located at 379.3 nm, and the absorption peak corresponding to the amorphous phase is not present. Figure 8b shows the UV absorption bands for the prepared samples with various pH values. The samples with an amorphous/crystalline composite structure (TZ3$_8$, TZ3$_{10}$, and TZ3$_{12}$) exhibit two absorption edges, but these edges are not very obvious for the TZ3$_4$ and TZ3$_6$ sample. It is obvious that the number of the absorption peaks increases from one to two with the pH increases, which is consistent with the change rule of the crystalline structure of the samples, as confirmed by the XRD and TEM results, the characteristic of the amorphous/crystalline heterostructure also becomes evident with increasing pH. Thus only the sample with amorphous/crystalline composite structure has two absorption bands, which could attributed to the amorphous/crystalline composite structure.

3.4. Enhanced Photocatalytic Properties. The photocatalytic activity of the samples was also evaluated for watersplitting. Fig. 9a displays H$_2$ production over samples without any noble metal cocatalyst. Obviously, the TZ3$_{12}$ sample shows the highest H$_2$ yield, reaching 8648 μmol after 8 h of irradiation with no signs of decay. And the photocatalytic activity of TZ3$_{12}$ sample is also far higher than that of the control samples (pure TiO$_2$). Moreover, the sample with amorphous/crystalline composite structure also showed a higher the H$_2$ productivity of when it is compared with some other similar works with or without noble metals cocatalyst.[49−54] Figure 9b shows the
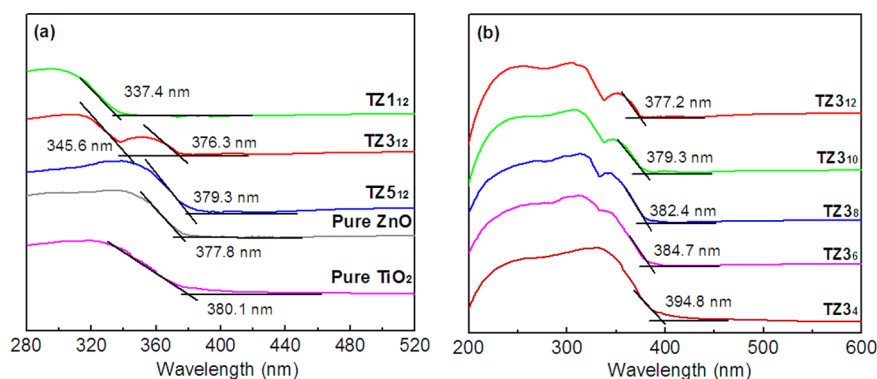

Figure 7. FT-IR spectra of the prepared samples.

Figure 8. UV−vis absorption bands for the prepared samples with (a) various Ti/Zn ratios (TZ1$_{12}$, TZ3$_{12}$ and TZ5$_{12}$) and (b) various pH values (TZ3$_4$, TZ3$_6$, TZ3$_8$, TZ3$_{10}$, and TZ3$_{12}$).
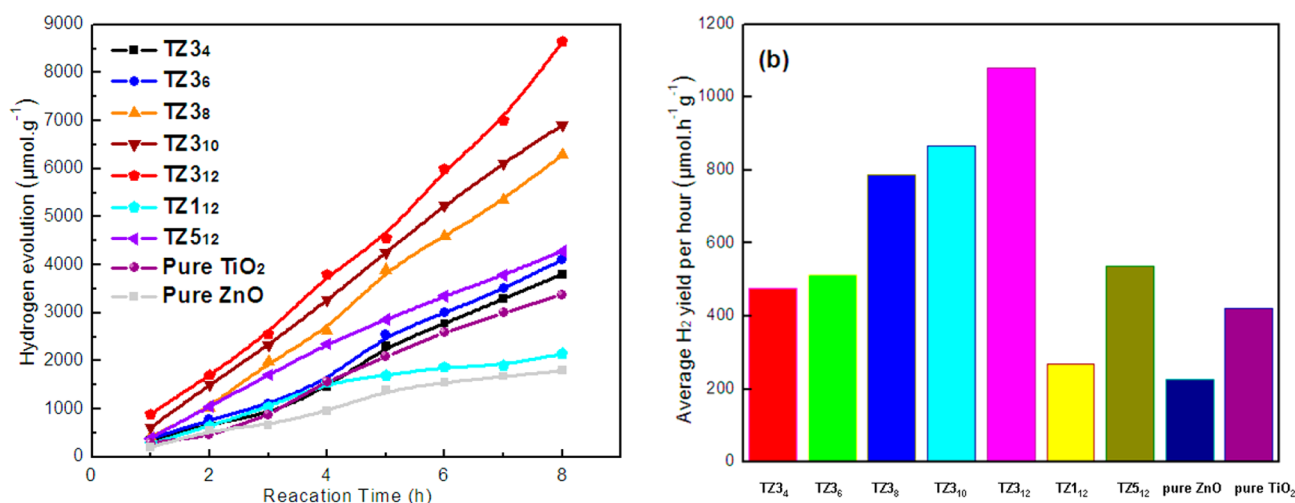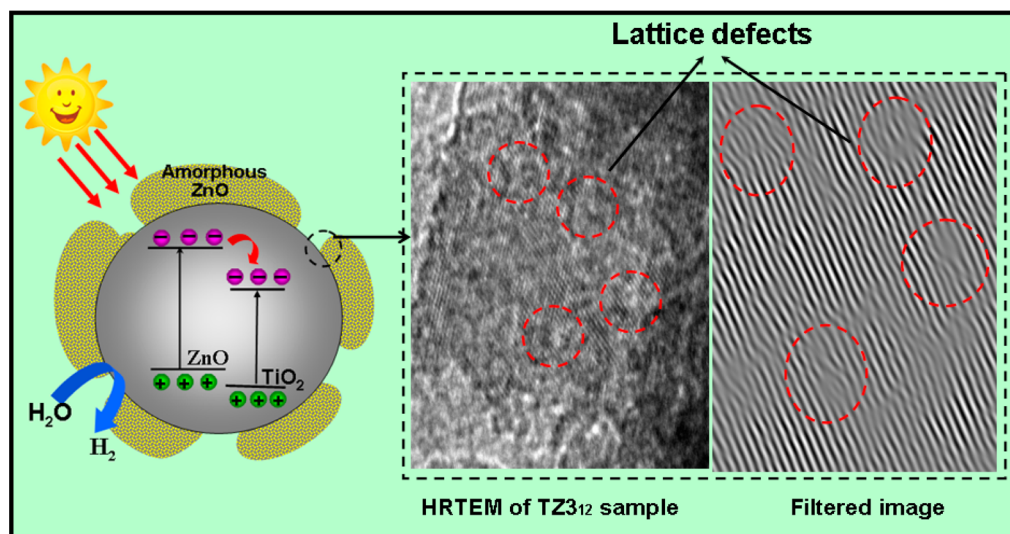

Figure 9. (a) Photocatalytic activity of ZnO/TiO$_2$ composite catalysts for hydrogen evolution from photocatalytic water splitting; (b) average hourly hydrogen evolution rates.

Scheme 1. Configuration Model of the Amorphous ZnO-Based Titania Heterostructure

average H$_2$ yield per hour. The average hydrogen production rate for TZ3$_{12}$ with an amorphous/crystalline composite structure reached 1081 μmol h^{-1} g^{-1}, which was nearly four times that for the amorphous structure. Figure S3 in the Supporting Information shows the photocatalytic activities of the samples under visible light irradiation, and the H$_2$ yield is not as good as the one under the xenon lamp irradiation (eg., TZ3$_{12}$), which could due to the band gaps of the samples did not show significant change based on the UV−vis results. Table 1 summarizes the H$_2$ production of the prepared samples.

4748

dx.doi.org/10.1021/am4054095 | ACS Appl. Mater. Interfaces 2014, 6, 4743−4751

3.5. Mechanism Analysis. Ohtani et al. has been reported that pure amorphous materials usually performs poor catalytic activity,[55] which is consist with the result of the above photocatalystic test. Although the H_2 production on $TZ5_{12}$, $TZ3_4$, and $TZ3_6$ is higher than that on $TZ1_{12}$, it is still much lower than that on $TZ3_8$, $TZ3_{10}$, and $TZ3_{12}$ (amorphous/crystallite composite structure). This indicates that the amorphous/crystallite composite structure could play an important role in photocatalytic activity. Thus, the overall photocatalytic H_2 evolution performance is dramatically improved with increasing pH value due to increasing prevalence of the amorphous/crystallite composite structure. Moreover, methanol, as a well-known sacrificial reagent, also plays an important role in the water splitting system. Figure S4 in the Supporting Information shows the role of the sacrificial reagents in the photocatalytic reactions, because methanol can trap photogenerated holes effectively, and thus methanol can act as a hole scavenger resulting in H_2 production.[56,57] In addition, it is interesting to note that the outer edge of the absorption onset of the sample exhibited a systematic blue shift in the UV-vis spectrum with increasing pH value. It is commonly assumed that red-shifted absorption peaks correspond to higher photocatalytic activity. However, there is no perfect correlation between the band-gap energy and photocatalytic activity in our results. We attribute the enhanced photocatalytic activity to the novel configuration of the amorphous/crystallite ZnO/TiO_2 heterostructure. There are a lot of lattice defects on the surface of the amorphous ZnO based titania heterostructure (a configuration model of the amorphous ZnO based titania composite structure is shown in Scheme 1), which serves as an electron trap by capturing electrons and promotes charge separation for the photocatalytic reaction. It is known that the activities of photocatalysts can often be enhanced by noble metal cocatalysts. However, the numerous unsaturated sites on the surface of amorphous ZnO-based titania composite structure could play the same role as the noble metal cocatalysts, as it is also in favor of the charge transfer and improves the separation of photogenerated electrons and holes. Moreover, it has been reported that adsorption and surface reactions occur more easily on amorphous surfaces than pure crystalline catalysts.[58] Samples with amorphous/crystallite composite structures have a large micropore area and BET surface area, which is conductive to absorbing more reagents and provides a large interface for photocatalytic reactions, facilitating the photocatalytic activity. Therefore, the samples with an amorphous/crystallite composite structure possess a favorable photocatalytic water-splitting capability.

4. CONCLUSIONS

In summary, we have developed a simple but efficient method for preparing a ZnO/TiO_2 amorphous/crystalline heterostructure with high photocatalytic activity for the generation of H_2 from photocatalytic water splitting without noble metal cocatalyst. It is interesting to note that the transformation of the amorphous/crystalline heterostructure can be controlled by modifying the pH value. The high-pH sample favors the formation of an amorphous-based titania heterostructure with a large BET surface area, while the weakly acidic sample favors the formation of pure anatase. Meanwhile, the sample at a pH of 12 has an amorphous/crystalline composite structure and exhibits the highest photocatalytic activity and the largest BET surface area. It is hoped that this work will lead to the better

utilization of amorphous structures to synthesize more efficient amorphous-based nanocomposite photocatalysts for H_2 generation from methanol/water-splitting.

■ ASSOCIATED CONTENT

Ⓢ Supporting Information

The experimental details, the information of the photocatalytic water splitting system, the Ti 2p XPS spectra of the $TZ1_{12}$, $TZ3_{12}$ and $TZ5_{12}$ sample (Figure S1), the description of the crystal structure (Figure S2), the photocatalytic activities of the samples under visible light irradiation (Figure S3), and the basic principle of photocatalytic reactions in the presence of sacrificial reagents (Figure S4). This material is available free of charge via the Internet at http://pubs.acs.org.

■ AUTHOR INFORMATION

Corresponding Author

*E-mail: songh77@hotmail.com.

Notes

The authors declare no competing financial interest.

■ ACKNOWLEDGMENTS

■ REFERENCES

(1) Kandiel, T. A.; Ismailac, A. A.; Bahnemann, D. W. Mesoporous TiO_2 Nanostructures: A Route to Minimize Pt Loading on Titania Photocatalysts for Hydrogen Production. *Phys. Chem. Chem. Phys.* **2011**, *13*, 20155−20161.

(2) Pai, Y. H.; Tsai, C. T.; Fang, S. Y. Enhanced Photocatalytic Hydrogen Generation with Pt Nanoparticles on Multi-Phase Polycrystalline Microporous MnO_2 Photocatalyst. *J. Power Sources* **2013**, *223*, 107−113.

(3) Kuang, Q.; Yang, S. H. Template Synthesis of Single-Crystal-Like Porous $SrTiO_3$ Nanocube Assemblies and Their Enhanced Photocatalytic Hydrogen Evolution. *ACS Appl. Mater. Interfaces* **2013**, *5*, 3683−3690.

(4) Guo, S. Y.; Han, S.; Chi, B.; Pu, J.; Li, J. Synthesis of Shape-Controlled Mesoporous Titanium Phosphate Nanocrystals: The hexagonal titanium Phosphate with Enhanced Hydrogen Generation from Water Splitting. *Int J Hydrogen Energy* **2014**, *39*, 2446−2453.

(5) Sreethawong, T.; Junbua, C.; Chavadej, S. Photocatalytic H_2 Production From Water Splitting under Visible Light Irradiation Using Eosin Y-sensitized Mesoporous-Assembled Pt/TiO_2 Nanocrystal Photocatalyst. *J. Power Sources* **2009**, *190*, 513−524.

(6) Ahmed, A. Y.; Kandiel, T. A.; Oekermann, T.; Bahnemann, D. Photocatalytic Activities of Different Well-Defined Single Crystal TiO_2 Surfaces: Anatase Versus Rutile. *J. Phys. Chem. Lett.* **2011**, *2*, 2461−2465.

(7) Fateh, R.; Dillert, R.; Bahnemann, D. Preparation and Characterization of Transparent Hydrophilic Photocatalytic TiO_2/SiO_2 Thin Films on Polycarbonate. *Langmuir* **2013**, *29*, 3730−3739.

(8) Nowotny, J.; Bak, T.; Nowotny, M. K.; Sheppard, L. R. Titanium Dioxide for Solar-Hydrogen I. Functional properties. *Int J Hydrogen Energy* **2007**, *32*, 2609−2629.

(9) Zhang, J. Y.; Wang, Y. H.; Zhang, J.; Yu, J. G. Enhanced Photocatalytic Hydrogen Production Activities of Au-Loaded ZnS Flowers. *ACS Appl. Mater. Interfaces* **2013**, *5*, 1031−1037.

(10) Reyes-Gil, K. R.; Robinson, D. B. WO₃-Enhanced TiO₂ Nanotube Photoanodes for Solar Water Splitting with Simultaneous Wastewater Treatment. *ACS Appl. Mater. Interfaces* **2013**, *5*, 12400−12410.

(11) Guo, S. Y.; Han, S.; Mao, H. F.; Dong, S. M.; Chi, B.; Pu, J.; Li, J. Structurally Controlled ZnO/TiO₂ Heterostructures as Efficient Photocatalysts for Hydrogen Generation from Water Without Noble Metals: The Role of Microporous Amorphous/Crystalline Composite Structure. *J. Power Sources* **2014**, *245*, 979−985.

(12) Reyes-Gil, K. R.; Wiggenhorn, C.; Brunschwig, B. S.; Lewis, N. S. Comparison between the Quantum Yields of Compact and Porous WO₃ Photoanodes. *J. Phys. Chem. C* **2013**, *117*, 14947−14957.

(13) Wang, X. W.; Liu, G.; Lu, G. Q.; Cheng, H. M. Stable Photocatalytic Hydrogen Evolution from Water over ZnO−CdS Core−Shell Nanorods. *Int. J. Hydrogen Energy* **2010**, *35*, 8199−8205.

(14) Guo, S. Y.; Han, S.; Wu, C. C.; Chi, B.; Pu, J.; Li, J. Synthesis and Characterization of Nitrogen and Phosphate Codoped Titanium Dioxide with Excellent Visible−Light Photocatalytic Activity. *J. Alloys Compd.* **2012**, *544*, 50−54.

(15) Regonini, D.; Teloeken, A. C.; Alves, A. K.; Berutti, F. A.; Gajda-Schrantz, K.; Bergmann, C. P.; Graule, T.; Clemens, F. Electrospun TiO₂ Fiber Composite Photoelectrodes for Water Splitting. *ACS Appl. Mater. Interfaces* **2013**, *5*, 11747−11755.

(16) Pan, K.; Dong, Y. Z.; Zhou, W.; Pan, Q. J.; Xie, Y.; Xie, T. F.; Tian, G. H.; Wang, G. F. Facile Fabrication of Hierarchical TiO₂ Nanobelt/ZnO Nanorod Heterogeneous Nanostructure: An Efficient Photoanode for Water Splitting. *ACS Appl. Mater. Interfaces* **2013**, *5*, 8314−8320.

(17) Regonini, D.; Adamaki, V.; Bowen, C. R.; Pennock, S. R.; Taylor, J.; Dent, A. C. E. AC Electrical Properties of TiO₂ and Magnéli Phases, Ti_nO_{2n-1}. *Solid State Ionics* **2012**, *229*, 38−44.

(18) Jang, J. S.; Kim, H. G.; Borse, P. H.; Lee, J. S. Simultaneous Hydrogen Production and Decomposition of H₂S Dissolved in Alkaline Water over CdS-TiO₂ Composite Photocatalysts under Visible Light Irradiation. *Int. J. Hydrogen Energy* **2007**, *32*, 4786−4791.

(19) Guo, S. Y.; Han, S.; Mao, H. F.; Zeng, C. H.; Sun, Y.; Chi, B.; Pu, J.; Li, J. Synthesis of Phosphorus-Doped Titania with Mesoporous Structure and Excellent Photocatalytic Activity. *Mater. Res. Bull.* **2013**, *48*, 3032−3036.

(20) Martha, S.; Das, D. P.; Biswal, N.; Parida, K. M. Facile Synthesis of Visible Light Responsive V₂O₅/N,S−TiO₂ Composite Photocatalyst: Enhanced Hydrogen Production and Phenol Degradation. *J. Mater. Chem.* **2012**, *22*, 10695−10703.

(21) Hara, M.; Hitoki, G.; Takata, T.; Kondo, J. N. TaON and Ta₃N₅ as New Visible Light Driven Photocatalysts. *Catal Today* **2003**, *78*, 555−560.

(22) Zong, X.; Yan, H. J.; Wu, G. P.; Ma, G. J.; Wen, F. Y. N.; Wang, L. Enhancement of Photocatalytic H₂ Evolution on CdS by Loading MoS₂ as Cocatalyst under Visible Light Irradiation. *J. Am. Chem. Soc.* **2008**, *130*, 7176−7167.

(23) Wang, Y. G.; Li, B.; Zhang, C. L.; Cui, L. F.; Kang, S. F.; Li, X.; Zhou, L. H. Ordered Mesoporous CeO₂-TiO₂ Composites: Highly Efficient Photocatalysts for the Reduction of CO₂ with H₂O under Simulated Solar Irradiation. *Appl. Catal. B* **2013**, *130*, 277−284.

(24) Xu, M. M.; Wang, J. F.; Tian, J. T.; Wang, X.; Dai, J. H.; Liu, X. Y. Hydrothermal and Post-Heat Treatments of TiO₂/ZnO Composite Powder and Its Photodegradation Behavior on Methyl Orange. *Ceram. Int.* **2011**, *37*, 2201−2206.

(25) Wang, N.; Sun, C.; Zhao, Y.; Zhou, S.; Chen, P.; Jiang, L. Fabrication of Three-Dimensional ZnO/TiO₂ Heteroarchitectures via a Solution Process. *J. Mater. Chem.* **2008**, *18*, 3909−3911.

(26) Lei, J. F.; Li, L. B.; Shen, X. H.; Du, K.; Li, W. S. Fabrication of Ordered ZnO/TiO₂ Heterostructures via a Templating Technique. *Langmuir* **2013**, *29*, 13975−13981.

(27) Liu, R. L.; Ye, H. Y.; Xiong, X. P.; Liu, H. Q. Fabrication of TiO₂/ZnO Composite Nanofibers by Electrospinning and Their Photocatalytic Property. *Mater. Chem. Phy.* **2010**, *121*, 432−439.

(28) Zou, C. W.; Yan, X. D.; Han, J.; Chen, R. Q.; Bian, J. M.; Haemmerle, E.; Gao, W. Preparation and Enhanced Photoluminescence Property of Ordered ZnO/TiO₂ Bottlebrush Nanostructures. *Chem. Phys. Lett.* **2009**, *476*, 84−88.

(29) Law, M.; Greene, L. E.; Radenovic, A.; Kuykendall, T.; Liphardt, J.; Yang, P. D. ZnO-Al₂O₃ and ZnO-TiO₂ Core-Shell Nanowire Dye-Sensitized Solar Cells. *J. Phys. Chem. B* **2006**, *110*, 22652−22663.

(30) Greene, L. E.; Law, M.; Yuhas, B. D.; Yang, P. D. ZnO-TiO₂ Core−Shell Nanorod/P3HT Solar Cells. *J. Phys. Chem. C* **2007**, *111*, 18451−18456.

(31) Cao, H.; Sui, S. L. Highly Efficient Heterogeneous Photo-oxidation of 2-Propanol to Acetone with Amorphous Manganese Oxide Catalysts. *J. Am. Chem. Soc.* **1994**, *116*, 5334−5342.

(32) Yan, J. M.; Zhang, X. B.; Han, S.; Shioyama, H.; Xu, Q. Iron-Nanoparticle-Catalyzed Hydrolytic Dehydrogenation of Ammonia Borane for Chemical Hydrogen Storage. *Angew. Chem., Int. Ed.* **2008**, *47*, 2287−2289.

(33) Cui, L. F.; Ruffo, R.; Chan, C. K.; Peng, H. L.; Cui, Y. Crystalline-Amorphous Core−Shell Silicon Nanowires for High Capacity and High Current Battery Electrodes. *Nano Lett.* **2009**, *9*, 491−495.

(34) Zhang, X. B.; Yan, J. M.; Han, S.; Shioyama, H.; Xu, Q. Magnetically Recyclable Fe@Pt Core−Shell Nanoparticles and Their Use as Electrocatalysts for Ammonia Borane Oxidation: The Role of Crystallinity of the Core. *J. Am. Chem. Soc.* **2009**, *131*, 2778−2779.

(35) Chen, Y. J.; Gao, P.; Wang, R. X.; Zhu, C. L.; Wang, L. J.; Cao, M. S.; Jin, H. B. Crystalline-Amorphous Core−Shell Silicon Nanowires for High Capacity and High Current Battery Electrodes. *J. Phys. Chem. C* **2009**, *113*, 10061−10064.

(36) Ismail, A. A.; Bahnemannb, D. W. Mesoporous Titania Photocatalysts: Preparation, Characterization and Reaction Mechanisms. *J. Mater. Chem.* **2011**, *21*, 11686−11707.

(37) Nandi, S. K.; Chatterjee, S.; Samanta, S. K.; Dalapati, G. K.; Bose, P. K.; Varma, S.; Shivprasad, P.; Maiti, C. K. Electrical Properties of Ta₂O₅ Films Deposited on ZnO. *Bull. Mater. Sci.* **2003**, *26*, 365−369.

(38) Tsai, M. T.; Chang, Y. U.; Huang, H. L.; Hsu, J. T.; Chen, Y. C.; Wu, A. Y. J. Characterization and Antibacterial Performance of Bioactive Ti−Zn−O Coatings Deposited on Titanium Implants. *Thin Solid Films* **2013**, *528*, 143−150.

(39) Bahadur, N. M.; Furusawa, T.; Sato, M.; Kurayama, F.; Suzuki, N. Rapid Synthesis, Characterization and Optical Properties of TiO₂ Coated ZnO Nanocomposite Particles by a Novel Microwave Irradiation Method. *Mater. Res. Bull.* **2010**, *45*, 1383−1388.

(40) Lastoskie, C.; Gubbins, K. E.; Quirke, N. Pore Size Distribution Analysis of Microporous Carbons: A Density Functional Theory Approach. *J. Phys, Chem.* **1993**, *97*, 4786−4796.

(41) Ivanova, T.; Harizanova, A.; Koutzarova, T.; Vertruyen, B. Preparation and Characterization of ZnO−TiO₂ Films Obtained by Sol-Gel Method. *J. Non-Cryst. Solids.* **2011**, *357*, 2840−2845.

(42) Liao, M. H.; Hsu, C. H.; Chen, D. H. Preparation and Properties of Amorphous Titania-Coated Zinc Oxide Nanoparticles. *J. Solid. State. Chem.* **2006**, *179*, 2020−2026.

(43) Wang, X. T.; Zhong, S. H.; Xiao, X. F. Photo-Catalysis of Ethane and Carbon Dioxide to Produce Hydrocarbon Oxygenates over ZnO-TiO₂/SiO₂ Catalyst. *J. Mol. Catal. A: Chem.* **2005**, *229*, 87−93.

(44) Xie, Y.; Liu, X.; Huang, A.; Ding, C.; Chu, P. K. Improvement of Surface Bioactivity on Titanium by Water and Hydrogen Plasma Immersion Ion Implantation. *Biomaterials* **2005**, *26*, 6129−6135.

(45) Music, S.; Gotic, M.; Ivanda, M.; Popovic, S.; Turkovic, A.; Trojko, R.; Sekulic, A.; Furic, K. Chemical and Micro Structural Properties of TiO₂ Synthesized by Sol-Gel Procedure. *Mater. Sci. Eng., B* **1997**, *47*, 33−40.

(46) Ocana, M.; Fornes, V.; Serna, J. V. Factors Affecting the Infrared and Raman Spectra of Rutile Powders. *J. Solid State Chem.* **1988**, *75*, 364−372.

4750

dx.doi.org/10.1021/am4054095 | *ACS Appl. Mater. Interfaces* 2014, 6, 4743−4751

(47) Djaoued, Y.; Badilescu, S.; Ashrit, P. V. Low Temperature Sol-Gel Preparation of Nanocrystalline TiO$_2$ Thin Films. *J Sol–Gel Sci. Technol.* **2002**, *24*, 247–254.

(48) Tian, J.; Wang, J.; Dai, J.; Wang, X.; Yin, Y. N-Doped TiO$_2$/ZnO Composite Powder and Its Photocatalytic Performance for Degradation of Methyl Orange. *Surf. Coat Technol.* **2009**, *204*, 723–730.

(49) Ismail, A. A.; Kandiel, T. A.; Bahnemann, D. W. Novel (and Better?) Titania-Based Photocatalysts: Brookite Nanorods and Mesoporous Structures. *J Photoch. Photobio. A* **2010**, *216*, 183–193.

(50) Yang, C. Y.; Wang, Z.; Lin, T. Q.; Huang, F. Q.; Xie, X. M.; Jiang, M. H. Core-Shell Nanostructured "Black" Rutile Titania as Excellent Catalyst for Hydrogen Production Enhanced by Sulfur Doping. *J. Am. Chem. Soc.* **2013**, *135*, 17831–17838.

(51) Liu, C.; Tang, J. Y.; Chen, H. M.; Liu, B.; Yang, P. D. A Fully Integrated Nanosystem of Semiconductor Nanowires for Direct Solar Water Splitting. *Nano Lett.* **2013**, *13*, 2989–2992.

(52) Alkaim, A. F.; Kandiel, T. A.; Hussein, F. H.; Dillerta, R.; Bahnemann, D. W. Solvent-Free Hydrothermal Synthesis of Anatase TiO$_2$ Nanoparticles with Enhanced Photocatalytic Hydrogen Production Activity. *Appl. Catal. A* **2013**, *466*, 32–37.

(53) Reyes-Gil, K. R.; Sun, Y. P.; Reyes-García, E.; Raftery, D. Characterization of Photoactive Centers in N-Doped In$_2$O$_3$ Visible Photocatalysts for Water Oxidation. *J. Phys. Chem. C* **2009**, *113*, 12558–12570.

(54) Guo, L.; Hagiwara, H.; Ida, S.; Daio, T.; Ishihera, T. One-Pot Soft-Templating Method to Synthesize Crystalline Mesoporous Tantalum Oxide and Its Photocatalytic Activity for Overall Water Splitting. *ACS Appl. Mater. Interfaces* **2013**, *5*, 11080–11086.

(55) Ohtani, B.; Ofawa, Y.; Nishimoto, S. I. Photocatalytic Activity of Amorphous-Anatase Mixture of Titanium(IV) Oxide Particles Suspended in Aqueous Solutions. *J. Phys. Chem. B* **1997**, *101*, 3746–3752.

(56) Kandiel, T. A.; Dillerta, R.; Robbenb, L.; Bahnemann, D. W. Photonic Efficiency and Mechanism of Photocatalytic Molecular Hydrogen Production over Platinized Titanium Dioxide from Aqueous Methanol Solutions. *Catal. Today* **2011**, *161*, 196–201.

(57) Oros-Ruiz, S.; Zanella, R.; López, R.; Hernández-Gordillo, A.; Gómez, R. Photocatalytic Hydrogen Production by Water/Methanol Decomposition Using Au/TiO$_2$ Prepared by Deposition–Precipitation with Urea. *J. Hazard. Mater.* **2013**, *263*, 2–10.

(58) Deng, J. F.; Li, H.; Wang, W. Progress in Design of New Amorphous Alloy Catalysts. *Catal. Today* **1999**, *51*, 113–125.